

# Extension of the entropy viscosity method to the low Mach regime for the multi-dimensional Euler equations

## Entropy-based viscous regularization for the multi-dimensional Euler equations in low-Mach regimes

Marc O. Delchini<sup>a</sup>, Jean C. Ragusa<sup>\*,a</sup>, Ray A. Berry<sup>b</sup>

<sup>a</sup>*Department of Nuclear Engineering, Texas A&M University, College Station, TX 77843, USA*

<sup>b</sup>*Idaho National Laboratory, Idaho Falls, ID 83415, USA*

---

### Abstract

The entropy viscosity method, introduced by Guermond et al. [1, 2], is extended to the multi-dimensional Euler equations for both subsonic (very low Mach numbers) and supersonic flows. We show that the current definition of the viscosity coefficients [1] is not adapted to low-Mach flows and we provide a robust alternate definition valid for any Mach number value. The new definitions are derived from a low-Mach asymptotic study. In addition, the entropy minimum principle is used to derive the viscous regularization terms for Euler equations with variable area for nozzle flow problems. Various 1- and 2-D numerical tests are presented : flow in a convergent-divergent nozzle, Leblanc shock tube, subsonic flow around a 2-D cylinder and over a circular hump, and supersonic flow in a compression corner. Convergence studies are performed using analytical solutions in 1-D. Both the ideal gas and stiffened gas equations of state are employed.

*Key words:* Euler equations with variable area, entropy viscosity method, stabilization method, low Mach regime, shocks.

---

### 1. Introduction

Over the past years an increasing interest raised for computational methods that can solve both compressible and incompressible flows. In engineering applications, there is often the need to solve for complex flows where a near incompressible regime or low Mach flow coexists with a supersonic flow domain. For example, such flow are encountered in aerodynamic in the study of airships.

---

<sup>\*</sup>Corresponding author

*Email addresses:* `delchmo@tamu.edu` (Marc O. Delchini), `jean.ragusa@tamu.edu` (Jean C. Ragusa), `ray.berry@inl.gov` (Ray A. Berry)

7 In the nuclear industry, flows are nearly the incompressible regime but com-  
8 pressible effects cannot be neglected because of the heat source and thus needs  
9 to be accurately resolved.

10 When solving the multi-D Euler equations for a wide range of Mach numbers,  
11 multiple problems have to address: stability, accuracy and acceleration of the  
12 convergence in the low Mach regime. Because of the hyperbolic nature of the  
13 equations, shocks can form during transonic and supersonic flows, and require  
14 the use of the numerical methods in order to stabilize the scheme and cor-  
15 rectly resolve the discontinuities. The literature offers a wide range of stabiliza-  
16 tion methods: flux-limiter [3, 4], pressure-based viscosity method ([5]), Lapidus  
17 method ([6, 7, 8]), and the entropy-viscosity method([1, 2]) among others. These  
18 numerical methods are usually developed using simple equation of states and  
19 tested for transonic and supersonic flows where the disparity between the acous-  
20 tic waves and the fluid speed is not large since the Mach number is of order one.  
21 This approach leads to a well-known accuracy problem in the low Mach regime  
22 where the fluid velocity is smaller than the speed of sound by multiple order of  
23 magnitude. The numerical dissipative terms become ill-scaled in the low Mach  
24 regime and lead to the wrong numerical solution by changing the nature of the  
25 equations solved. This behavior is well documented in the literature [9, 10, 11]  
26 and often treated by performing a low Mach asymptotic study of the multi-D  
27 Euler equation. This method was originally used [9] to show convergence of the  
28 compressible multi-D Euler equations to the incompressible ones. Thus, by us-  
29 ing the same method, the effect of the dissipative terms in the low Mach regime,  
30 can be understood and, when needed, a fix is developed in order to ensure the  
31 convergence of the equations to the correct physical solution. This approach  
32 was used as a fixing method for multiple well known stabilization methods alike  
33 Roe scheme ([12]) and SUPG [11] while preserving the original stabilization  
34 properties of shocks.

35 We propose, through this paper, to investigate how the entropy viscosity method,  
36 when applied to the multi-D Euler equations with variable area, behaves in the  
37 low Mach regime. This method was initially introduced by Guermond et al.  
38 to solve for the hyperbolic systems and has shown good results when used for  
39 solving the multi-D Euler equations with various discretization schemes. More  
40 importantly, it is simple to implement, can be used with unstructured grids,  
41 and its dissipative terms are consistent with the entropy minimum principle  
42 and proven valid for any equation of state under certain conditions [13].

43 This paper is organized as follows: in Section 2 the current definition of the en-  
44 tropy viscosity method is recalled, and inconsistency with the low Mach regime  
45 are pointed out. Since our interest is in the variable area version of the multi-D  
46 Euler equation, the reader is guided through the steps leading to the derivation  
47 of the dissipative terms on the model of [13]. Then in Section 3, a new definition  
48 of the viscosity coefficient is introduced and derived from a low Mach asymp-  
49 totic study. After detailing the spatial and temporal discretization method in  
50 Section 4, 1- and 2-D numerical results are presented in Section 5 for a wide  
51 range of Mach numbers: low Mach flow over a cylinder and a circular bump,  
52 and supersonic flow in a compression corner [14]. Convergence studies are per-

53 formed in 1-D, in order to demonstrate the accuracy of the solution.  
 54 For purpose of clarity, the multi-D Euler equations with variable area are re-  
 55 called in Eq. (1) and the corresponding variables are defined:

$$\begin{cases} \partial_t (\rho A) + \vec{\nabla} \cdot (\rho \vec{u} A) = 0 \\ \partial_t (\rho \vec{u} A) + \vec{\nabla} \cdot [(\rho \vec{u} \otimes \vec{u} + P \mathbf{I}) A] = P \vec{\nabla} A \\ \partial_t (\rho E A) + \vec{\nabla} \cdot [\vec{u} (\rho E + P) A] = 0 \\ P = P(\rho, e) \end{cases} \quad (1)$$

56 where  $\rho$ ,  $\rho \vec{u}$  and  $\rho E$  are the density, the momentum and the total energy, re-  
 57 spectively, and will be referred to as the conservative variables. The pressure  
 58  $P$  is computed with an equation of state expressed in function of the density  $\rho$   
 59 and the specific internal energy  $e$ . The tensor product  $\vec{a} \otimes \vec{b}$  is taken with the  
 60 following convention:  $(\vec{a} \otimes \vec{b})_{i,j} = a_i b_j$ . Lastly, the terms  $\partial_t$ ,  $\vec{\nabla}$ ,  $\vec{\nabla} \cdot$  and  $\mathbf{I}$  denote  
 61 the temporal derivative, the gradient and divergent operators, and the identity  
 62 tensor, respectively. The variable area  $A$  is assumed spatial dependent.

## 63 2. The Entropy Viscosity Method

### 64 2.1. Background

65 In this section, the entropy-based viscosity method [1, 2, 15] is recalled for  
 66 the multi-D Euler equations (with constant area  $A$ ) [16]. The entropy-based  
 67 viscosity method consists of adding dissipative terms, with a viscosity coeffi-  
 68 cient modulated by the entropy production which allows high-order accuracy  
 69 when the solution is smooth. Thus, two questions arise: (i) how are the viscos-  
 70 ity dissipative terms derived and (ii) how to numerically compute the entropy  
 71 production. Answers to the first question can be found in [13] by Guermond et  
 72 al., that details the proof leading to the derivation of the artificial dissipative  
 73 terms (Eq. (2)) consistent with the entropy minimum principle theorem. The  
 74 viscous regularization obtained is valid for any equation of state as long as the  
 75 opposite of the physical entropy function,  $s$ , is convex with respect to the in-  
 76 ternal energy  $e$  and the specific volume  $1/\rho$ . As for the entropy production, it  
 77 is locally evaluated by computing the local entropy residual  $D_e(\vec{x}, t)$  defined in  
 78 Eq. (4), that is known to be peaked in shocks [17].

$$\begin{cases} \partial_t (\rho) + \vec{\nabla} \cdot (\rho \vec{u}) = \vec{\nabla} \cdot (\kappa \vec{\nabla} \rho) \\ \partial_t (\rho \vec{u}) + \vec{\nabla} \cdot (\rho \vec{u} \otimes \vec{u} + P \mathbf{I}) = \vec{\nabla} \cdot (\mu \rho \vec{\nabla}^s \vec{u} + \kappa \vec{u} \otimes \vec{\nabla} \rho) \\ \partial_t (\rho E) + \vec{\nabla} \cdot [\vec{u} (\rho E + P)] = \vec{\nabla} \cdot (\kappa \vec{\nabla} (\rho e) + \frac{1}{2} \|\vec{u}\|^2 \kappa \vec{\nabla} \rho + \rho \mu \vec{u} \vec{\nabla} \vec{u}) \\ P = P(\rho, e) \end{cases} \quad (2)$$

79 where  $\kappa$  and  $\mu$  are local positive viscosity coefficients.  $\vec{\nabla}^s \vec{u}$  denotes the sym-  
 80 metric gradient operator that guarantees the method to be rotational invariant  
 81 [13].

82 In the current version of the method,  $\kappa$  and  $\mu$  are set equal, so that the above

viscous regularization (Eq. (2)) is equivalent to the parabolic regularization [18] when considering the 1-D form of the equation. The current definition includes a first-order viscosity coefficient referred to with the subscript  $max$ , and a high-order viscosity coefficient referred to with the subscript  $e$ . The first-order viscosity coefficients  $\mu_{max}$  and  $\kappa_{max}$  are proportional to the local largest eigenvalue  $\|\vec{u}\| + c$  and equivalent to an upwind-scheme (see Eq. (3)), when used, which is known to be over-dissipative and monotone [17]:

$$\mu_{max}(\vec{r}, t) = \kappa_{max}(\vec{r}, t) = \frac{h}{2} (\|\vec{u}\| + c), \quad (3)$$

where  $h$  is defined as the ratio of the grid size to the polynomial order of the test functions used.

The second-order viscosity coefficients  $\kappa_e$  and  $\mu_e$  are set proportional to the entropy production that is evaluated by computing the local entropy residual  $D_e$ . It also includes the interfacial jump of the entropy flux  $J$  that will allow to detect any discontinuities other than shocks:

$$\mu_e(\vec{r}, t) = \kappa_e(\vec{r}, t) = h^2 \frac{\max(|D_e(\vec{r}, t)|, J)}{\|s - \bar{s}\|_\infty} \quad \text{with } D_e(\vec{r}, t) = \partial_t s + \vec{u} \cdot \vec{\nabla} s \quad (4)$$

where  $\|\cdot\|_\infty$  and  $\bar{\cdot}$  denote the infinite norm operator and the average operator over the entire computational domain, respectively. The definition of the jump  $J$  is discretization-dependent and examples of definition can be found in [16] for DGFEM. The denominator  $\|s - \bar{s}\|_\infty$  is used for dimensionality purposes and should not be of the same order as  $h$ , on penalty of losing the high-order accuracy. Currently, there are no theoretical justification for choosing the denominator.

The definition of the viscosity coefficients  $\mu$  and  $\kappa$  is function of the first- and second-order viscosity coefficients as follows:

$$\mu(\vec{r}, t) = \min(\mu_e(\vec{r}, t), \mu_{max}(\vec{r}, t)) \quad \text{and} \quad \kappa(\vec{r}, t) = \min(\kappa_e(\vec{r}, t), \kappa_{max}(\vec{r}, t)). \quad (5)$$

This definition allows the following properties. In shock regions, the second-order viscosity coefficient experiences a peak because of entropy production, and thus, saturates to the first-order viscosity that is known to be over-dissipative and will smooth out oscillations. Anywhere else, the entropy production being small, the viscosity coefficients  $\mu$  and  $\kappa$  are of order  $h^2$ .

Using the above definition of the entropy-based viscosity method, high-order accuracy was demonstrated and excellent results were obtained with 1-D Sod shock tubes and various 2-D tests [1, 2, 16].

## 2.2. Issues in the Low-Mach Regime

In the Low-Mach Regime, the flow is known to be isentropic resulting in very little entropy production. Since the entropy viscosity method is directly based on the evaluation of the local entropy production, it will be interested to study how the entropy viscosity coefficients  $\mu$  and  $\kappa$  scale in the low Mach

regime. Mathematically, it means that the entropy residual  $D_e$  will be very small, so will be the denominator  $\|s - \bar{s}\|_\infty$ , thus making the ratio, used in the definition of the viscosity coefficients Eq. (4), undetermined. Therefore, the current definition of the viscosity coefficients seems unadapted to subsonic flow and could lead to ill-scaled dissipative terms. A solution would be to recast the entropy residual as a function of other variables in order to have more freedom in the choice of the normalization parameter. With this approach, the viscosity coefficients are still defined proportional to the entropy residual that is a good indicator of the flow type (subsonic, transonic and supersonic flow). Plus, a different normalization parameter could be chosen, based on a low Mach asymptotic study so that the viscosity coefficients are well-scaled in the low Mach asymptotic limit (see Section 3).

### 2.3. The dissipative-terms for the multi-D Euler equations with variable area

One of the focus of this paper is to investigate the application of the entropy viscosity method to the multi-D Euler equations with variable area. The variable area version of the Euler equations is mostly used in 1-D and 2-D for obvious reasons, and differs from Eq. (1) by the momentum equation as shown in Eq. (6), that contains a non-conservative term proportional to the area gradient. For the purpose of this paper, the variable area is assumed to be a smooth function and only spatial dependent. An example can be found in [19] where a fluid flows through a 1-D convergent-divergent nozzle and reaches a steady-state solution.

$$\begin{cases} \partial_t (\rho A) + \vec{\nabla} \cdot (\rho \vec{u} A) = 0 \\ \partial_t (\rho \vec{u} A) + \vec{\nabla} \cdot [A (\rho \vec{u} \otimes \vec{u} + P \mathbf{I})] = P \vec{\nabla} A \\ \partial_t (\rho E) + \vec{\nabla} \cdot [\vec{u} (\rho E + P)] = 0 \end{cases} \quad (6)$$

The application of the entropy viscosity method to the above system of equations is expected to be straightforward since it degenerates to the Eq. (1) when assuming a constant area. Details of the derivations of the dissipative terms are available to the reader in Appendix B and are very similar to what was done in [13]. An entropy residual is derived without the dissipative terms. Then, the same entropy residual is re-derived after adding dissipative terms to each equation of the system given in Eq. (6), and the entropy minimum principle is used as a condition to obtain a definition for each of the dissipative terms. The final result including the dissipative terms is given in Eq. (7):

$$\begin{cases} \partial_t (\rho A) + \vec{\nabla} \cdot (\rho \vec{u} A) = \vec{\nabla} \cdot (A \kappa \vec{\nabla} \rho) \\ \partial_t (\rho \vec{u} A) + \vec{\nabla} \cdot [A (\rho \vec{u} \otimes \vec{u} + P \mathbf{I})] = P \vec{\nabla} A + \vec{\nabla} \cdot \left[ A \left( \mu \rho \vec{\nabla}^s \vec{u} + \kappa \vec{u} \otimes \vec{\nabla} \rho \right) \right] \\ \partial_t (\rho E) + \vec{\nabla} \cdot [\vec{u} (\rho E + P)] = \vec{\nabla} \cdot \left[ A \left( \kappa \vec{\nabla} (\rho e) + \frac{1}{2} \|\vec{u}\|^2 \kappa \vec{\nabla} \rho + \rho \mu \vec{u} \vec{\nabla} \vec{u} \right) \right] \end{cases} \quad (7)$$

The dissipative terms are very similar to the ones obtained for the multi-D Euler equations: each dissipative flux is multiplied by the variable area  $A$  in order to ensure conservation of the flux. When assuming a constant area, Eq. (2) is retrieved. The definition of the viscosity coefficients  $\mu$  and  $\kappa$  is explained in Section 3.2.

### 153 3. All-speed Reformulation of the Entropy Viscosity Method

154 In this section, the entropy residual  $D_e$  is recast as a function of the pressure,  
 155 the density and the speed of sound. Then, a low Mach asymptotic study of the  
 156 multi-D Euler equations is performed in order to derive the correct normalization  
 157 parameter.

#### 158 3.1. New Entropy Production Residual

159 The first step in defining a viscosity coefficient that behaves well in the low  
 160 mach limit is to recast the entropy residual in terms of the thermodynamic  
 161 variables as shown in Eq. (8):

$$D_e(\vec{r}, t) = \partial_t s + \vec{u} \cdot \vec{\nabla} s = \frac{s_e}{P_e} \left( \underbrace{\frac{dP}{dt} - c^2 \frac{d\rho}{dt}}_{\tilde{D}_e(\vec{r}, t)} \right), \quad (8)$$

162 where  $\frac{d}{dt}$  denotes the material or total derivative, and  $P_e$  is the partial derivative  
 163 of pressure with respect to internal energy. The steps that lead to the new  
 164 formulation of the entropy residual  $D_e$  can be found in Appendix A.

165 The entropy residual  $D_e$  and  $\tilde{D}_e$  are proportional to each other and therefore  
 166 will experience the same variation when taking the absolute value. Thus, locally  
 167 evaluating  $\tilde{D}_e$  instead of  $D_e$  should allow us to measure the entropy production  
 168 point wise. This new expression given in Eq. (8) has multiple advantages:

- 169 • an analytical expression of the entropy function is not longer needed: the  
 170 entropy residual  $\tilde{D}_e$  is evaluated using the local values of the pressure, the  
 171 density and the speed of sound. Deriving an entropy function for some  
 172 complex equation of states can be difficult.
- 173 • with the proposed expression of the entropy residual function of pressure  
 174 and density, additional normalizations suitable for low Mach flows of the  
 175 entropy residual can be devised. Examples include the pressure itself,  
 176 or combination of the density, the speed of sound and the norm of the  
 177 velocity:  $\rho c^2$ ,  $\rho c ||\vec{u}||$  and  $\rho ||\vec{u}||^2$ .

178 The viscosity coefficients  $\mu$  and  $\kappa$  are now defined proportional to the new  
 179 entropy residual  $\tilde{D}_e$  on the model of Eq. (4) as follows:

$$\mu(\vec{r}, t) = \kappa(\vec{r}, t) = h^2 \frac{\max(\tilde{D}_e, J)}{n(P)} \quad (9)$$

180 where  $n(P)$  is a normalization parameter to determine and all other variables  
 181 were defined previously.

182 As mentioned earlier, the normalization parameter  $n(P)$  must be of the same  
 183 units as the pressure for the viscosity coefficients to have the unit of a dy-  
 184 namic viscosity ( $m^2/s$ ). Multiples options are available to us:  $P$ ,  $\rho c^2$ ,  $\rho c ||\vec{u}||$

185 and  $\rho||\vec{u}||^2$ . The choice of the normalization parameter cannot be random if  
 186 the definition of the viscosity coefficient is wanted to be well-scaled for a wide  
 187 range of Mach numbers. For example, by choosing  $n(P) = \rho||\vec{u}||^2$ , the viscosity  
 188 coefficient will become very large as the Mach number decreases which would  
 189 be unnecessary since the equations will not develop any shock or discontinuity.  
 190 Therefore, it is proposed to carry, in Section 3.2, a low-Mach asymptotic study  
 191 of the multi-D Euler equations in order to determine the correct expression for  
 192 the normalization parameter  $n(P)$ .

### 193 3.2. Low-Mach asymptotic study of the multi-D Euler equations

194 The asymptotic study requires the multi-D Euler equations to be non di-  
 195 mensionalized: the objective is to make the Mach number appears and thus,  
 196 use a polynomial expansion of the variables as a function of the Mach number  
 197 in order to derive the leading, first- and second-order equations. Before detailing  
 198 the steps of the asymptotic method, let us have a closer look at the system of  
 199 equations under consideration. The initial system of equations is composed of  
 200 the multi-D Euler equations. For stability purpose, artificial dissipative terms  
 201 are added to each equation as explained in Section 2. The resulting system of  
 202 equations is alike the multi-D Navier-Stokes equations in a sense that it con-  
 203 tains second-order derivative terms. Thus, it would be interesting to look at the  
 204 steps employed in the asymptotic study of the multi-D Navier-Stokes equations  
 205 in order to understand how the dissipative terms are treated. Fortunately, this  
 206 process is well-documented in the literature [9, 10, 11] for both multi-D Eu-  
 207 ler equations and Navier-Stokes equations. The work presented here is mainly  
 208 inspired of [20] that focuses on the asymptotic study in the low Mach regime  
 209 of Navier-Stokes equations. During the derivation, the reader has to keep in  
 210 mind that the objective of this section is to derive a normalization parameter  
 211 for the definition of the viscosity coefficients so that the multi-D Euler equations  
 212 degenerate to the incompressible system of equations, which implies that the  
 213 dissipative terms are well-scaled. The main steps of the derivation are presented  
 214 in the following of this section:

215 To express Eq. (2) in dimensionless variables, the following dimensional variables  
 216 are introduced:

$$\begin{aligned} \rho &= \frac{\rho^*}{\rho_\infty}, P = \frac{P^*}{\rho_\infty c_\infty^2}, \mu = \frac{\mu^*}{\mu_\infty}, E = \frac{E^*}{c_\infty^2}, \mu = \frac{\mu^*}{\mu_\infty}, \\ \kappa &= \frac{\kappa^*}{\kappa_\infty}, x = \frac{x^*}{L_\infty}, t = \frac{t^*}{L_\infty/u_\infty}, u = \frac{u^*}{u_\infty} \end{aligned} \quad (10)$$

217 where the subscript  $\infty$  and the upper script  $*$  denote the far field or stagnation  
 218 quantities and the dimensionless variables, respectively. The reference quantities  
 219 are chosen such that the non dimensional flow quantities are of order one for  
 220 any low reference-Mach number

$$M_\infty = \frac{u_\infty^*}{c_\infty^*} \quad (11)$$

221 where  $c_\infty^*$  is a reference value for the speed of sound.  
 222 Then, using the non dimensional quantities and the multi-D Euler equations  
 223 from Eq. (2) , the following non dimensional form is obtained:

$$\left\{ \begin{array}{l} \partial_t \rho + \nabla \cdot (\rho \vec{u}) = \frac{1}{Re_\infty Pr_\infty} \nabla \cdot (\kappa \nabla \rho) \\ \partial_t (\rho \vec{u}) + \nabla \cdot (\rho \vec{u} \otimes \vec{u}) + \frac{1}{M_\infty^2} \nabla (P) = \frac{1}{Re_\infty} \nabla (\rho \mu \nabla \vec{u}) + \frac{1}{Re_\infty Pr_\infty} \nabla \cdot (\vec{u} \otimes \kappa \nabla \rho) \\ \partial_t (\rho E) + \nabla \cdot [\vec{u} (\rho E + P)] = \frac{1}{Re_\infty Pr_\infty} \nabla \cdot (\kappa \nabla (\rho e)) + \frac{M_\infty^2}{Re_\infty} \nabla \cdot (\vec{u} \rho \mu \nabla \vec{u}) \\ + \frac{M_\infty^2}{2 Re_\infty Pr_\infty} \nabla \cdot (\kappa u^2 \nabla \rho) \\ P = (\gamma - 1) (\rho E + M_\infty^2 \rho u^2) \end{array} \right.$$

224 where the *numerical* Reynolds ( $Re_\infty$ ) and Prandtl ( $Pr_\infty$ ) numbers are defined  
 225 as follows:

$$Re_\infty = \frac{u_\infty L_\infty}{\mu_\infty} \text{ and } Pr_\infty = \frac{\mu_\infty}{\kappa_\infty}. \quad (12)$$

226 Since it is chosen to have the same definition for both  $\mu$  and  $\kappa$  the numerical  
 227 Prandtl number is unconditionally equal to one:  $Pr_\infty = 1$ .  
 228 Once the dimensionless equations are obtained, the next step consists of expand-  
 229 ing each variable in term of the Mach number (example given in Eq. (13) for  
 230 the pressure  $P$ ) in order to derive the leading, first- and second-order equations.

$$P(\vec{r}, t) = P_0(\vec{r}, t) + P_1(\vec{r}, t) M_\infty + P_2(\vec{r}, t) M_\infty^2 + \dots \text{ with } M_\infty \rightarrow 0 \quad (13)$$

231 Before deriving the leading-order equation, a choice needs to be made on how  
 232 the numerical Reynolds number scales. Multiple options are available to us and  
 233 a few example are given:  $Re_\infty = M_\infty$ , or  $Re_\infty = M_\infty^{-1}$  or  $Re_\infty = 1$ . Let us  
 234 assume for academy purpose that the numerical Reynolds number scales as the  
 235 inverse of the Mach number square:  $Re_\infty = M_\infty^{-2}$ . The best way to evaluate the  
 236 impact of this choice on the equations, is to look at the momentum equation  
 237 and try to derive the order  $M_\infty^{-2}$ :

$$\vec{\nabla} P_0 = \vec{\nabla} \cdot (\rho_0 \mu_0 \vec{\nabla} \vec{u}_0 + \vec{u}_0 \otimes \vec{\nabla} \rho_0) \quad (14)$$

238 which is known to be ([11])

$$\vec{\nabla} P_0 = 0 \quad (15)$$

239 It is clear that Eq. (14) and Eq. (15) will not yield the same result. The same  
 240 conclusion is drawn when deriving the order  $M_\infty^{-1}$  of the momentum equation,  
 241 making our initial assumption not suitable. From the above result, it is under-  
 242 stood that the numerical Reynolds number has to scale as one so that it does  
 243 not affect the orders  $M_\infty^{-2}$  and  $M_\infty^{-1}$  of the momentum equations:  $Re_\infty = 1$ .



244 Thus, with such assumption, Eq. (12) implies:

At order  $M_\infty^{-2}$ :

$$\vec{\nabla} P_0 = 0$$

At order  $M_\infty^{-1}$ :

$$\vec{\nabla} P_1 = 0$$

At leading-order:

$$\begin{aligned} \partial_t \rho_0 &+ \vec{\nabla} \cdot (\rho_0 \vec{u}_0) = \vec{\nabla} \cdot (\kappa_0 \vec{\nabla} \rho_0) \\ \partial_t (\rho_0 \vec{u}_0) &+ \vec{\nabla} \cdot (\rho_0 \vec{u}_0 \otimes \vec{u}_0) + \vec{\nabla} P_2 = \vec{\nabla} \cdot (\rho_0 \mu_0 \vec{\nabla} \vec{u}_0 + \vec{u}_0 \otimes \vec{\nabla} \rho_0) \\ \partial_t (\rho_0 E_0) &+ \vec{\nabla} \cdot [\vec{u}_0 (\rho_0 E_0 + P_0)] = \vec{\nabla} \cdot (\kappa_0 \vec{\nabla} (\rho_0 e_0)) \end{aligned}$$

245 Under this form, the dissipative terms only affect the leading-order equations  
246 in the asymptotic limit.

247 It is now determined that the numerical Reynolds number  $Re_\infty$  has to scale as  
248 one. Following Eq. (12),  $Re_\infty$  is a function of the  $\mu_\infty$ , and thus  $n_P$ . It can be  
249 shown using Eq. (10) and the definitions of  $\tilde{D}$  given in Eq. (8) that:

$$\mu_\infty = \frac{\rho_\infty c_\infty^2 u_\infty L}{n_{P,\infty}} \quad (16)$$

250 where  $n_{P,\infty}$  is the far-field quantity for the normalization parameter  $n_P$ . Sub-  
251 stituting Eq. (16) into Eq. (12) and remembering that the numerical Reynolds  
252 number scales as one, it yields:

$$n_{P,\infty} = \rho_\infty c_\infty^2 \quad (17)$$

253 Eq. (17) tells us that in the asymptotic limit, the normalization parameter  $n_P$   
254 scales as  $\rho_\infty c_\infty^2$  which leaves us with two options: either  $n_P = \rho c^2$  or  $n_P = P$ .  
255 The choice was made to use  $n_P = \rho c^2$  in the asymptotic limit: it was found  
256 to behave well and the pressure can become locally negative and null in some  
257 particular case as shown in Section 5. This normalization parameter is only valid  
258 in the asymptotic limit and the purpose of this paper is to define a viscosity  
259 coefficient  $\mu$  that is valid for a wide range of Mach numbers. Thus, it is proposed  
260 to define the high-order viscosity coefficient  $\mu_e$  as follows:

$$\mu_e = h^2 \frac{\max(\tilde{D}_e, J)}{(1 - f(M))\rho c^2 + f(M)\rho ||\vec{u}||^2} \quad (18)$$

261 where  $f(M)$  is a function of the local Mach number  $M$  with the following prop-  
262 erties:

$$\begin{cases} f(M) \rightarrow 0 \text{ as } M \rightarrow 0 \\ f(M) \rightarrow 1 \text{ as } M \geq 1 \end{cases} \quad (19)$$

263 The choice of the function  $f(M)$  is not fixed and a few examples are available  
264 in the literature. A simple definition is  $f(M) = \min(M, 1)$  which meets the  
265 conditions of Eq. (19). Another definition for  $f(M)$  was proposed by [12].

266 All of the numerical results presented in Section 5 were obtained by using  
 267  $f(M) = \min(M, 1)$  which is simple to implement. A convergence test for a  
 268 subsonic flow over a 2-D cylinder will show that this definition of  $f(M)$  yields  
 269 the correct behavior in the asymptotic limit. The definition of the high-order  
 270 viscosity coefficient  $\mu_e(\vec{r}, t)$  should behave well for complex flow where a near  
 271 incompressible regime coexists with a supersonic flow domain since  $f(M)$  is  
 272 function of the local Mach number.  
 273 For clarity purpose, the full definition of the viscosity coefficient  $\mu(\vec{r}, t)$  is re-  
 274 called:

$$\left\{ \begin{array}{l} \mu(\vec{r}, t) = \max(\mu_{max}(\vec{r}, t), \mu_e(\vec{r}, t)) \\ \text{where } \mu_{max}(\vec{r}, t) = \frac{h}{2}(|\vec{u}| + c) \\ \text{and } \mu_e(\vec{r}, t) = h^2 \frac{\max(\bar{D}_e, J)}{(1-f(M))\rho c^2 + f(M)\rho|\vec{u}|^2} \\ \mu(\vec{r}, t) = \kappa(\vec{r}, t) \end{array} \right. \quad (20)$$

275 These viscosity coefficients are valid for both the multi-D Euler equations with  
 276 variable and constant area and are employed with the dissipative terms detailed  
 277 in Eq. (12). The reader will notice that, through the derivation, none assumption  
 278 was made on the type of equation of state besides the convexity condition on  
 279 the entropy function  $s$ . The remaining of this paper (Section 5) will focus on  
 280 demonstrating that the definition of the viscosity coefficient given in Eq. (20) is  
 281 indeed well-scaled in the asymptotic limit and that shocks are still well resolved.

## 282 4. Solution Techniques Spatial and Temporal Discretizations

283 In order to detail the partial and temporal discretization used for this study,  
 284 the system of equations Eq. (7) is considered under the following form for sim-  
 285 plicity:

$$\partial_t U + \vec{\nabla} \cdot F(U) = S \quad (21)$$

286 where  $U$  is the vector solution,  $F$  is a conservative vector flux and  $S$  is a vector  
 287 source that can contain the non-conservative term  $P\vec{\nabla}A$ .

### 288 4.1. Spatial and Temporal Discretizations

289 The system of equation given in Eq. (21) is discretized using a continuous  
 290 Galerkin finite element method and high-order temporal integrators provided  
 291 by the MOOSE framework.

#### 292 4.1.1. CFEM

293 In order to apply the continuous finite element method, Eq. (21) is multiplied  
 294 by a smooth test function  $\phi$ , integrated by part and each integral is split onto  
 295 each finite element  $e$  of the discrete mesh  $\Omega$  bounded by  $\partial\Omega$ , to obtain a weak  
 296 solution:

$$\sum_e \int_e \partial_t U \phi - \sum_e \int_e F(U) \cdot \vec{\nabla} \phi + \int_{\partial\Omega} F(U) \vec{n} \phi - \sum_e \int_e S \phi = 0 \quad (22)$$

297 The integrals over the elements  $e$  are evaluated using quadrature-point rules.  
 298 The Moose framework provides a wide range of test function and quadrature  
 299 rules: trapezoidal and Gauss rules among others. Linear Lagrange polynomials  
 300 will be used as test functions and should ensure second-order convergence for  
 301 smooth functions. The order of convergence will be demonstrated.

#### 302 4.1.2. Temporal integrator

303 The MOOSE framework offers both first- and second-order explicit and im-  
 304 plicit temporal integrators. In all of the numerical examples presented in Sec-  
 305 tion 5, the time-dependent term  $\int_e \partial_t U \phi$  will be evaluated using the second-order  
 306 temporal integrator BDF2. By considering three solutions,  $U^{n-1}$ ,  $U^n$  and  $U^{n+1}$   
 307 at three different time  $t^{n-1}$ ,  $t^n$  and  $t^{n+1}$ , respectively, it yields:

$$\begin{aligned} \int_e \partial_t U \phi &= \int_e (\omega_0 U^{n+1} + \omega_1 U^n + \omega_2 U^{n-1}) \phi & (23) \\ \text{with } \omega_0 &= \frac{2\Delta t^{n+1} + \Delta t^n}{\Delta t^{n+1} (\Delta t^{n+1} + \Delta t^n)}, \\ \omega_1 &= -\frac{\Delta t^{n+1} + \Delta t^n}{\Delta t^{n+1} \Delta t^n} \\ \text{and } \omega_2 &= \frac{\Delta t^{n+1}}{\Delta t^n (\Delta t^{n+1} + \Delta t^n)} \end{aligned}$$

308 where  $\Delta t^n = t^n - t^{n-1}$  and  $\Delta t^{n+1} = t^{n+1} - t^n$ .

#### 309 4.2. Boundary conditions

310 The boundary conditions will be treated by either using Dirichlet or Neu-  
 311 mann conditions. The multi-D Euler equations are wave-dominated systems  
 312 that require great care when dealing with boundary conditions. It is often rec-  
 313 ommended to use the characteristic equations to compute the correct flux at the  
 314 boundaries. Our implementation of the subsonic boundary conditions will fol-  
 315 low the method described in [19] that was developed for Ideal Gas and Stiffened  
 316 Gas equation of states. For each numerical solution presented in Section 5, the  
 317 type of boundary conditions used will be specified and taken among the follow-  
 318 ings: supersonic inlet, subsonic inlet (stagnation pressure boundary), supersonic  
 319 outlet and subsonic inlet (static pressure boundary).

#### 320 4.3. Solver

321 A Free-Jacobian-Newton-Krylov (FJNK) method is used to solve for the  
 322 solution at each time step. The jacobian matrix of the discretized equations  
 323 was derived by hand, hard coded and used as a preconditioner. This method  
 324 requires the partial derivative of the pressure with respect to the conservative  
 325 variables to be known. The contribution of the artificial dissipative terms to  
 326 the jacobian matrix is simplified by assuming constant viscosity coefficients as  
 327 shown in Eq. (24) for the dissipative terms of the continuity equation:

$$\frac{\partial}{\partial U_i} \left( \kappa \vec{\nabla} \rho \vec{\nabla} \phi \right) = \kappa \frac{\partial}{\partial U_i} (\rho) \vec{\nabla} \phi \quad (24)$$

where  $U_i$  denotes the set of conservative variables.

## 5. Numerical Results

This section is dedicated to presenting 1- and 2-D numerical results obtained by solving Eq. (7) with the entropy viscosity method. This section has two objectives: validate our new definition of the viscosity coefficients for the low Mach limit, and, make sure that the new definition can still resolve shocks.

The first set of 1-D simulations consist of liquid water and steam flowing in a convergent-divergent nozzle. This test is interesting for multiple reasons: a steady-state is reached (some stabilization methods are known to have difficulties to reach a steady-state ([3, 4])), it can be performed for liquid and gas phases, and, an analytical solution of the steady-state solution is available which allow for convergence study. The 1-D Leblanc shock tube test [21] (in a straight pipe) is also performed and consists of a flow developing shocks. A convergence study will be performed in order to demonstrate convergence of the numerical solution to the exact solution.

This section also included 2-D simulations from subsonic to supersonic flows. Subsonic flows of a gas over a 2-D cylinder and a hump [22] are simulated and results are shown for various far-field Mach numbers. Numerical results of a supersonic flow in a compression corner are provided to illustrate the capabilities of the new definition in the supersonic case. Convergence studies are performed when an analytical solution is available.

For each simulation, informations relative to the boundary conditions and the equation of state will be provided. All of the numerical solution presented in this section are run with the second-order temporal integrator *BDF2* and linear polynomials test functions. The integrals are numerically computed using a second-order Gauss quadrature rule. The Ideal Gas [23] or Stiffened Gas equation of state [24] are used and a generic formulation is recalled in Eq. (25).

$$P = (\gamma - 1)\rho(e - q) - \gamma P_\infty \quad (25)$$

where the parameters  $q$  and  $P_\infty$  are fluid dependent and will be specified in time. Eq. (25) degenerates to the Ideal Gas equation of state by setting  $q$  and  $P_\infty$  to zero. The Ideal and Stiffened Gas equation of states have a convex entropy  $s$ :

$$s = C_v \ln \left( \frac{P + P_\infty}{\rho^{\gamma-1}} \right)$$

### 5.1. Liquid water in a 1-D divergent-convergent nozzle

The simulation consists of liquid water flowing through a 1-D convergent-divergent nozzle with the following equation,  $A(x) = 1 + 0.5 \cos(2\pi x/L)$ , where  $L = 1m$  is the length of the nozzle. At the inlet, the stagnation pressure and temperature are set to  $P_0 = 1MPa$  and  $T_0 = 453K$ , respectively. At the outlet, only the static pressure is specified:  $P_s = 0.5MPa$ . Details about the theory related to the inlet and outlet boundary conditions can be found in [19].

Initially, the temperature is uniform and set equal to the stagnation temperature and the pressure linearly decreases from the stagnation pressure to the static one. Finally, the liquid is assumed at rest. The Stiffened Gas equation of state is used to model the liquid water with the parameters provided in Table 1.

Table 1: Stiffened Gas Equation of State parameters for liquid water.

$\gamma$	$C_v (J \cdot kg^{-1} \cdot K^{-1})$	$P_\infty (Pa)$	$q (J \cdot kg^{-1})$
2.35	1816	$10^9$	$-1167.10^3$

Because of the low pressure difference between the inlet and the outlet, and the large value of  $P_\infty$ , the flow remains subsonic and thus, should not display any shock. Enthalpy and entropy are conserved through the nozzle, and these conservation relations are used to determine the exact solution at steady-state [25]. Plots of the velocity, density and pressure are given at steady-state in Fig. 1a, Fig. 1b, Fig. 1c, respectively, along with the exact solution for comparison. The viscosity coefficients are also plotted in Fig. 1d. The mesh used is uniform and has 50 cells.

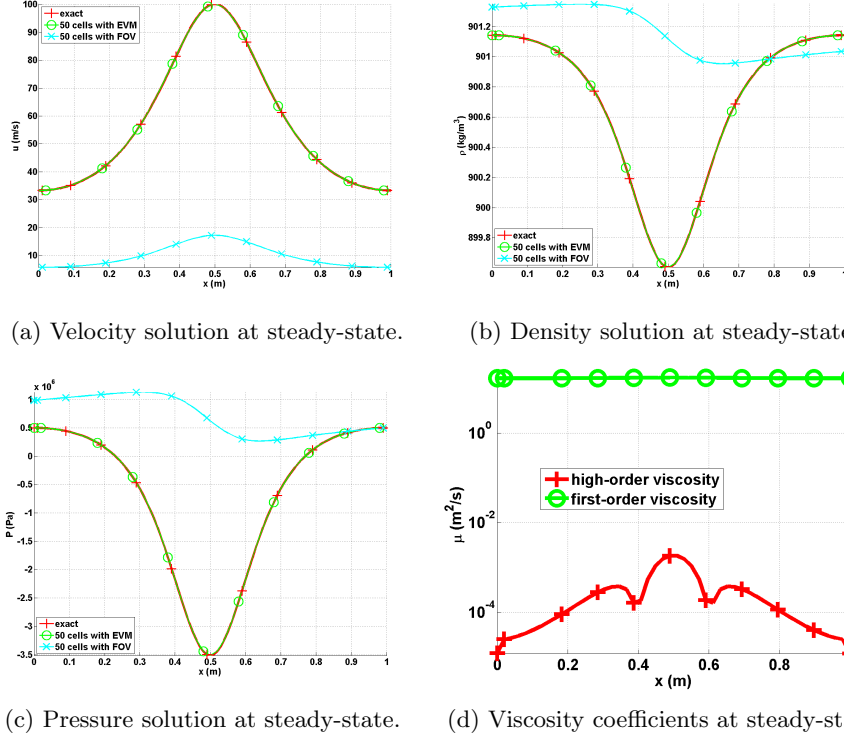


Figure 1: Steady-state solution for liquid phase in a 1-D convergent-divergent nozzle with an uniform mesh of 50 cells.

In Fig. 1, the numerical solutions of the pressure, velocity and density obtained with the first-order viscosity (FOV) and the entropy viscosity method (EVM) are plotted against the exact solution. A fairly coarse mesh (50 cells) was used. The numerical solution obtained with the EVM and the exact solution perfectly overlap. On the other hand, the numerical solution run with the FOV does not give the correct steady-state: this is an illustration of the effect of ill-scaled dissipative terms. It is also noted that the second-order viscosity coefficient is very small compare to the first-order one as expected (Fig. 1d): (i) the numerical solution is smooth as shown in Fig. 1 and (ii) the flow is in a low Mach regime and thus isentropic. A convergence study was performed using the exact solution as a reference: the L1 and L2 norms of the error and the corresponding convergence rates are computed at steady-state on various uniform mesh from 4 to 256 cells. The results for linear polynomials  $Q_1$  are reported in Table 2 and Table 3 for the primitive variables: density, velocity and pressure.

Table 2: L1 norm of the error for the liquid phase in a 1-D convergent-divergent nozzle at steady-state.

cells	density	rate	pressure	rate	velocity	rate
4	$2.8037 \cdot 10^{-1}$	—	$8.4705e \cdot 10^5$	—	7.2737	—
8	$1.3343 \cdot 10^{-1}$	1.0713	$4.7893e \cdot 10^5$	0.24227	6.1493	0.074683
16	$2.9373 \cdot 10^{-2}$	2.1835	$1.0613e \cdot 10^5$	2.3247	1.2275	2.4501
32	$5.1120 \cdot 10^{-3}$	2.5225	$1.8446 \cdot 10^4$	2.6959	$1.8943 \cdot 10^{-1}$	3.0966
64	$1.0558 \cdot 10^{-3}$	2.2755	$3.7938 \cdot 10^3$	2.3207	$3.7919 \cdot 10^{-2}$	2.3323
128	$2.3712 \cdot 10^{-4}$	2.1547	$8.4471 \cdot 10^2$	2.0624	$8.5517 \cdot 10^{-3}$	2.0473
256	$5.6058 \cdot 10^{-5}$	2.0806	$1.9839 \cdot 10^2$	2.0478	$2.0475 \cdot 10^{-3}$	1.9833
512	$1.3278 \cdot 10^{-5}$	2.0778	46.622	2.0478	$4.9516 \cdot 10^{-4}$	1.9669

Table 3: L2 norm of the error for the liquid phase in a 1-D convergent-divergent nozzle at steady-state.

cells	density	rate	pressure	rate	velocity	rate
4	$3.106397 \cdot 10^{-1}$	—	$5.254445 \cdot 10^5$	—	3.288543	—
8	$7.491623 \cdot 10^{-2}$	2.07	$1.636966 \cdot 10^5$	1.60	1.823880	0.90
16	$2.079858 \cdot 10^{-2}$	1.80	$4.627338 \cdot 10^4$	1.75	$4.990605 \cdot 10^{-1}$	1.83
32	$5.329627 \cdot 10^{-3}$	1.90	$1.180287 \cdot 10^4$	1.92	$1.261018 \cdot 10^{-1}$	1.93
64	$1.341583 \cdot 10^{-3}$	1.94	$2.967104 \cdot 10^3$	1.98	$3.160914 \cdot 10^{-2}$	1.99
128	$3.359766 \cdot 10^{-4}$	1.99	$7.428087 \cdot 10^2$	1.99	$7.907499 \cdot 10^{-3}$	1.99
256	$8.403859 \cdot 10^{-5}$	1.99	$1.857861 \cdot 10^2$	1.99	$1.977292 \cdot 10^{-3}$	1.99
512	$2.10075 \cdot 10^{-5}$	1.99	27.048	1.99	$4.9516 \cdot 10^{-4}$	1.99

It is observed that the convergence rate for the L1 and L2 norm of the error is 2: the entropy viscosity method conserves the high-order accuracy when the numerical solution is smooth, and the new definition of the entropy viscosity coefficient seems to behave as expected in the low Mach limit.

## 5.2. Steam in a 1-D divergent-convergent nozzle

Instead of liquid water, we now simulate a flow of steam using the exact same 1-D geometry, initial conditions and boundary conditions as in Section 5.1. The Stiffened gas equation of state is still used but with different parameters that are given in Table 4: steam is a gas and compressible effects will become dominant.

Table 4: Stiffened Gas Equation of State parameters for steam.

$\gamma$	$C_v \ (J \cdot kg^{-1} \cdot K^{-1})$	$P_\infty \ (Pa)$	$q \ (J \cdot kg^{-1})$
1.43	1040	0	$2030 \cdot 10^3$

401 The pressure difference applied between the inlet and outlet is large enough  
 402 to make the steam accelerates through the nozzle and result in the formation of  
 403 shock in the divergent part. The behavior is different from what is observed for  
 404 the liquid water phase in Section 5.1 because of the liquid to gas density ratio  
 405 that is of 1000. Even though a shock forms, an exact solution at steady-state  
 406 is still available [25]. The objective of this section is to show that using the  
 407 new definition of the viscosity coefficient in Eq. (20), the shock can be correctly  
 408 resolved without spurious oscillation. The steady-state numerical solution is  
 409 shown in Fig. 2 and was run with a mesh of 1600 cells.

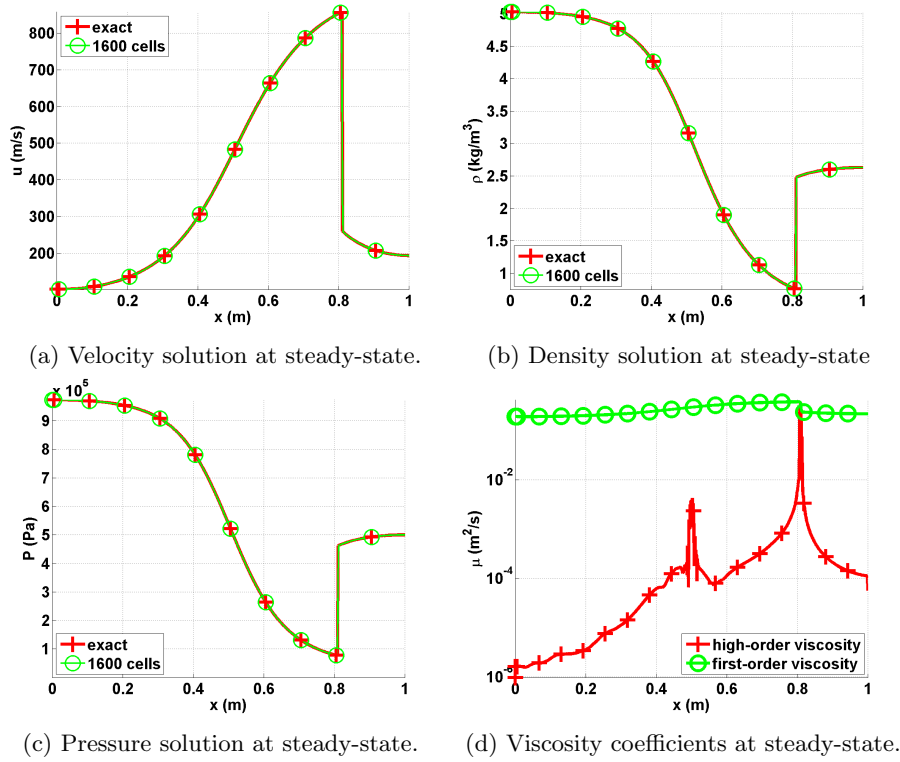


Figure 2: Steady-state solution for vapor phase in a 1-D convergent-divergent nozzle.

410 The steady-state solution of the density, velocity and pressure are given  
 411 in Fig. 2a, Fig. 2b and Fig. 2c. The steady-solution displays a shock around  
 412  $x = 0.8m$  and match the exact solution. In Fig. 2d, the first- and second-  
 413 order viscosity coefficients are log plotted at steady-state: the second-order  
 414 viscosity coefficient is peaked in the shock region around  $x = 0.8m$  as expected,  
 415 and saturate to the first-order viscosity coefficient. The profile also displays  
 416 another peak at  $x = 0.5m$  that corresponds to the position of the sonic point



for a 1-D convergent-divergent nozzle: this particular point is known to develop small instabilities that are detected when computing the jumps of the pressure and density gradients. Anywhere else, the second-order viscosity coefficient is small. In order to prove convergence of the numerical solution to the exact solution, a convergence study is performed. Because of the presence of a shock, second-order accuracy cannot be achieved. However, the convergence rate of a numerical solution containing a shock is known and expected to be of 1 and 1/2 when computing the L1 and L2 norms of the error, respectively (see Theorem 9.3 in [26]). Results are reported in Table 5 and Table 6 for the primitive variables: density, velocity and pressure.

Table 5: L1 norm of the error for the vapor phase in a 1-D convergent-divergent nozzle at steady-state.

cells	density	rate	pressure	rate	velocity	rate
5	$0.72562 \cdot 10^{-1}$	—	$1.5657 \cdot 10^5$	—	173.69	—
10	$0.4165 \cdot 10^{-1}$	0.80088	$9.6741 \cdot 10^4$	0.63425	120.69	0.52519
20	$0.20675 \cdot 10^{-1}$	1.0104	$4.9193 \cdot 10^4$	0.96971	72.149	0.74228
40	$0.093703 \cdot 10^{-1}$	1.1417	$2.0103 \cdot 10^4$	0.72728	34.716	1.0554
80	$0.047328 \cdot 10^{-1}$	0.9854	$1.0208 \cdot 10^4$	0.9777	16.082	1.1101
160	$0.023965 \cdot 10^{-2}$	0.9817	$5.1969 \cdot 10^3$	0.9739	7.9573	1.0150
320	$0.020768 \cdot 10^{-2}$	0.9886	$2.5116 \cdot 10^3$	1.0490	3.7812	1.0734
640	$0.0059715 \cdot 10^{-2}$	1.0160	$1.2754 \cdot 10^3$	0.9776	1.8353	1.0428

Table 6: L2 norm of the error for the vapor phase in a 1-D convergent-divergent nozzle at steady-state.

cells	density	rate	pressure	rate	velocity	rate
5	$9.7144 \cdot 10^{-1}$	—	$2.0215 \cdot 10^5$	—	236.94	—
10	$5.9718 \cdot 10^{-1}$	0.70195	$1.3024 \cdot 10^5$	0.63425	166.56	0.50854
20	$2.9503 \cdot 10^{-1}$	1.0173	$6.6503 \cdot 10^4$	0.96971	103.36	0.68831
40	$1.8193 \cdot 10^{-1}$	0.69747	$4.0171 \cdot 10^4$	0.72728	66.374	0.6390
80	$1.3366 \cdot 10^{-1}$	0.44485	$2.3163 \cdot 10^4$	0.43576	42.981	0.62692
160	$9.6638 \cdot 10^{-2}$	0.46790	$1.7263 \cdot 10^4$	0.42413	31.717	0.43844
320	$7.0896 \cdot 10^{-2}$	0.44688	$1.2763 \cdot 10^4$	0.43571	23.138	0.45499
640	$5.2191 \cdot 10^{-2}$	0.44190	$9.4217 \cdot 10^3$	0.43790	16.910	0.45238

The convergence rates for the L1 and L2 norms of the error are close to the theoretical values which prove convergence of the numerical solution to the exact solution.

It is also interesting to investigate the effect of the first-order viscosity onto the steady-state solution. In Fig. 3, the steady-state velocity profile is plotted when using the first- and second-order viscosity coefficients: the main difference

433 between the two numerical solution is in the resolution of the shock around  
 434  $x = 0.8m$ . The first-order viscosity coefficient is by definition more dissipative  
 435 and will smooth out the solution. In the other hand, the high-order viscosity  
 436 better resolves the shock and allow high-order accuracy away from the shock  
 437 region. It is also noted that the numerical solution obtained with the first-order  
 438 viscosity coefficient is satisfying: this is due to the nature of the solution that  
 439 contains a standing shock, and thus, will force the shock to form even with large  
 440 artificial dissipation.

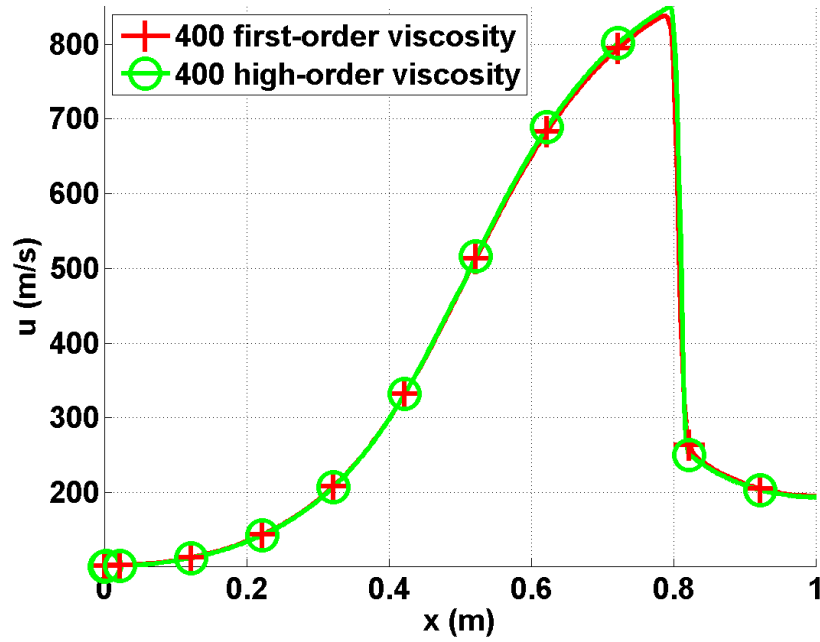


Figure 3: Velocity profile at steady-state with the first- and second-order viscosity for a mesh with 400 cells.

### 441 5.3. Leblanc shock tube

442 The 1-D Leblanc shock tube is a Riemann problem designed to test the  
 443 robustness and the accuracy of the stabilization method. The initial conditions  
 444 are given in Table 7. The ideal gas equation of state is used to compute the  
 445 fluid pressure with the following heat capacity ratio  $\gamma = 5/3$ .

Table 7: Initial conditions for the 1-D Leblanc shock tube.

	$\rho$	$u$	$e$
left	1.	0.	0.1
right	$10^{-3}$	0.	$10^{-7}$

446 This test is computationally challenging because of the large left to right  
 447 pressure ratio. The computational domain consists of a 1-D pipe of length  
 448  $L = 9m$  with an interface located at  $x = 2m$ . At  $t = 0.s$ , the interface is  
 449 removed, allowing the fluid to move. The numerical solution is run until  $t = 4.s$   
 450 and the density, momentum and total energy profiles are given in Fig. 4a, Fig. 4b  
 451 and Fig. 4c, respectively, along with the exact solution. The viscosity coefficients  
 452 are also plotted in Fig. 4d. These plots were run with three different uniform  
 453 mesh of 800, 3200 and 6000 cells and a constant time step  $\Delta t = 10^{-3}s$ .

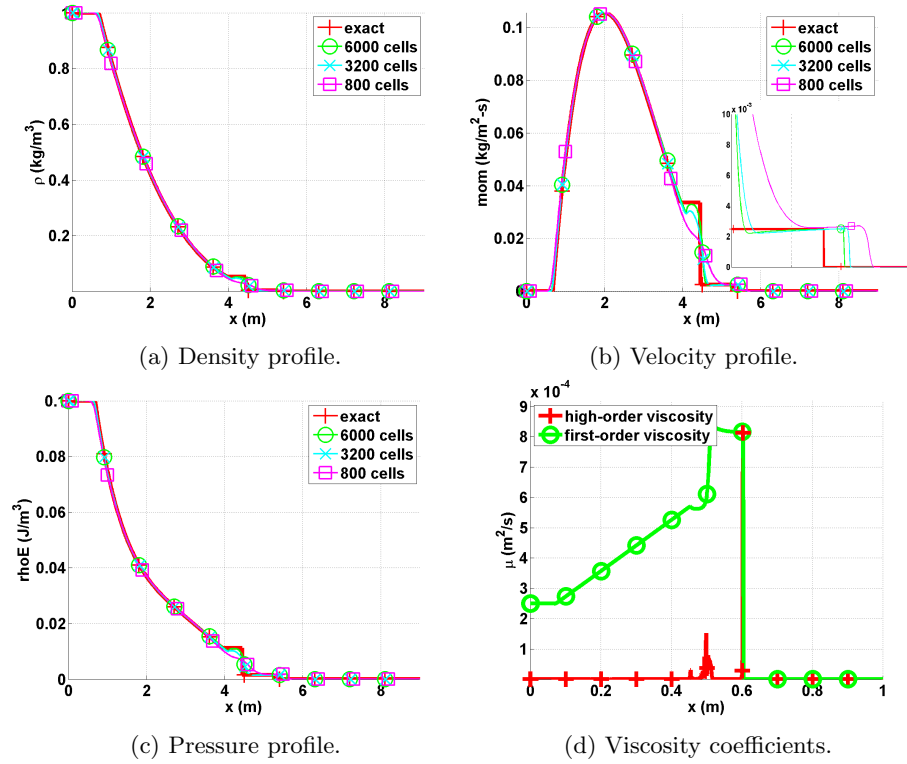


Figure 4: Numerical solution for the 1-D Leblanc shock tube at  $t = 4.s$ .

454 The density, momentum and total energy profiles given in Fig. 4 do not  
 455 display any oscillations. In Fig. 4b, the shock region is zoomed in for better  
 456 resolution: the shock is well resolved and do not show any oscillation. It is

457 also observed that the shock position of the numerical solution converges to the  
 458 exact position when refining the mesh. The contact wave is shown in Fig. 4b at  
 459  $x = 4.5m$ . The second-order viscosity coefficient profile is shown in Fig. 4d and  
 460 behaves as expected: it saturates to the first-order viscosity in the shock region  
 461 and thus prevent oscillations from forming. In the contact wave at  $x = 4.5m$ , a  
 462 smaller peak is observed that is due to the presence of the jumps in the definition  
 463 of the second-order viscosity coefficient (Eq. (20)).  
 464 Once again, a convergence study is performed in order to prove convergence of  
 465 the numerical solution to the exact solution. As for the vapor phase in the 1-D  
 466 nozzle (Section 5.2), the expected convergence rate for the L1 and L2 norms  
 467 of the error are 1 and  $1/2$ , respectively. The exact solution was obtained by  
 468 running a 1-D Riemann solver and used as a reference solution to compute the  
 469 L1 and L2-norms of the error that are reported in Table 8 and Table 9 for the  
 470 conservative variables: density, momentum and total energy.

Table 8: L1 norm of the error for the 1-D Leblanc test at  $t = 4.s$ .

cells	density	rate	momentum	rate
100	$1.0354722 \cdot 10^{-2}$	—	$3.5471714 \cdot 10^{-3}$	—
200	$7.2680512 \cdot 10^{-3}$	0.51064841	$2.5933119 \cdot 10^{-3}$	0.45187331
400	$5.0825628 \cdot 10^{-3}$	0.51601245	$2.0668092 \cdot 10^{-3}$	0.32739054
800	$3.4025056 \cdot 10^{-3}$	0.57895861	$1.4793838 \cdot 10^{-3}$	0.48240884
1600	$2.1649953 \cdot 10^{-3}$	0.65223363	$9.7152832 \cdot 10^{-4}$	0.6066684
3200	$1.2465433 \cdot 10^{-3}$	0.79643094	$5.5937409 \cdot 10^{-4}$	0.79644263
6400	$6.4476928 \cdot 10^{-4}$	0.95107804	$3.0244198 \cdot 10^{-4}$	0.88715502
12800	$3.3950948 \cdot 10^{-4}$	0.92533116	$1.5958118 \cdot 10^{-4}$	0.9223679

cells	total energy	rate
100	0.0014033046	—
200	$9.8611746 \cdot 10^{-4}$	0.5089968
400	$7.7844421 \cdot 10^{-4}$	0.34116585
800	$5.5702549 \cdot 10^{-4}$	0.48285029
1600	$3.5720171 \cdot 10^{-4}$	0.64100438
3200	$2.0491799 \cdot 10^{-4}$	0.80169235
6400	$1.0914891 \cdot 10^{-4}$	0.90874889
12800	$5.7909794 \cdot 10^{-5}$	0.91441847

Table 9: L2 norm of the error for the 1-D Leblanc test at  $t = 4.s$ .

cells	density	rate	momentum	rate
100	$5.7187851 \cdot 10^{-3}$	—	$1.7767236 \cdot 10^{-3}$	—
200	$3.8995238 \cdot 10^{-3}$	0.55241073	$1.4913161 \cdot 10^{-3}$	0.25263314
400	$2.8103526 \cdot 10^{-3}$	0.4725468	$1.3305301 \cdot 10^{-3}$	0.164585
800	$2.1081933 \cdot 10^{-3}$	0.41474398	$1.1398931 \cdot 10^{-3}$	0.22310254
1600	$1.5731052 \cdot 10^{-3}$	0.42239201	$9.0394227 \cdot 10^{-4}$	0.33459602
3200	$1.0610667 \cdot 10^{-3}$	0.56809979	$6.2735595 \cdot 10^{-4}$	0.52694639
6400	$7.3309974 \cdot 10^{-4}$	0.53343397	$4.4545754 \cdot 10^{-4}$	0.49399631
12800	$5.1020991 \cdot 10^{-4}$	0.52291857	$3.1266758 \cdot 10^{-4}$	0.5106583

cells	total energy	rate
100	$7.6112265 \cdot 10^{-4}$	—
200	$5.5497308 \cdot 10^{-4}$	0.45571115
400	$4.6063172 \cdot 10^{-4}$	0.26880405
800	$3.7798953 \cdot 10^{-4}$	0.28526749
1600	$2.9584646 \cdot 10^{-4}$	0.35349763
3200	$2.054455 \cdot 10^{-4}$	0.52609289
6400	$1.4670834 \cdot 10^{-4}$	0.48580482
12800	$1.0299897 \cdot 10^{-5}$	0.51032105

The convergence rates are close to the expected values which prove convergence of the numerical solution to the exact solution.

#### 5.4. Subsonic flow over a 2-D cylinder

The flow of a fluid over a 2-D cylinder is a typical benchmark case to test the behavior of a numerical method in the low Mach regime. For this test, an analytical solution is available in the incompressible limit or low Mach limit (REFS) and often referred to as potential flow. The main features of the potential flow are the following:

- The solution is symmetric: the iso-mach number lines are used to assess the symmetry of the numerical solution.
- The velocity at the top of the cylinder is twice the incoming velocity set at the inlet.
- The pressure fluctuations are proportional to the inlet Mach number square, as follows:

$$\tilde{P} = \frac{\max(P) - \min(P)}{\max(P)} \propto M_{\infty}^2$$

where  $\tilde{P}$  and  $M_{\infty}$  are the pressure fluctuations and the inlet Mach number, respectively.

487 The computational domain consists of a  $1 \times 1$  square with a circular hole of radius  
 488 0.05 in its middle. At the inlet, a subsonic stagnation boundary condition is  
 489 used: the stagnation pressure and temperature are computed using the following  
 490 relations, valid for the Stiffened and Ideal gas equation of states:

$$\begin{cases} P_0 = P \left(1 + \frac{\gamma-1}{2} M^2\right)^{\frac{\gamma}{\gamma-1}} \\ T_0 = T \left(1 + \frac{\gamma-1}{2} M^2\right) \end{cases} \quad (26)$$

491 The static pressure  $P_s = 101325 \text{ Pa}$  is set at the subsonic outlet and a static  
 492 pressure boundary type is used. The implementation of the pressure boundary  
 493 conditions is done on the model of [19]. A solid wall boundary condition is set for  
 494 the top and bottom walls of the computational domain: the normal velocity is  
 495 zero since no mass can penetrate the solid body. The mesh is made of triangular  
 496 cells.

497 The steady-state for Mach numbers ranging from  $M_\infty = 10^{-3}$  to  $M_\infty = 10^{-7}$   
 498 is shown in Fig. 5. The iso-Mach lines are drawn with 50 intervals ranging from  
 499  $10^{-8}$  to  $2M_\infty$ , and allow to assess the symmetry of the numerical solution.

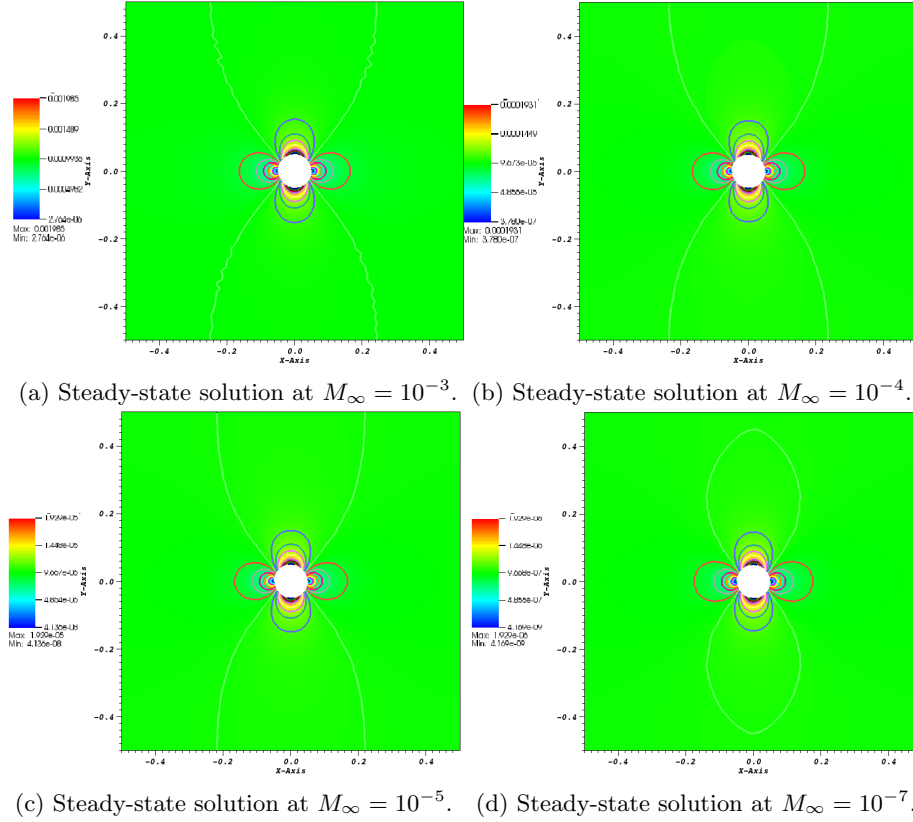


Figure 5: Steady-state solution for a subsonic flow over a 2-D cylinder.

500 In Table 10, the velocity at the top of the cylinder and at the inlet are given  
501 for the different values of the Mach number presented in Fig. 5. The ratio of  
502 the inlet velocity to the velocity at the top of cylinder is also computed and is  
503 very close to 2 as expected.

Table 10: Velocity ratio for different Mach numbers.

Mach number	inlet velocity	velocity at the top of the cylinder	ratio
$10^{-3}$	$2.348 \cdot 10^{-3}$	$1.176 \cdot 10^{-3}$	1.99
$10^{-4}$	$2.285 \cdot 10^{-4}$	$1.145 \cdot 10^{-4}$	1.99
$10^{-5}$	$2.283 \cdot 10^{-5}$	$1.144 \cdot 10^{-5}$	1.99
$10^{-6}$	$2.283 \cdot 10^{-6}$	$1.144 \cdot 10^{-6}$	1.99
$10^{-7}$	$2.283 \cdot 10^{-7}$	$1.144 \cdot 10^{-7}$	1.99

504 In Fig. 6, the pressure and velocity fluctuations are plotted as a function  
505 of the far field Mach number, on a log-log plot. The pressure and velocity  
506 fluctuations are expected to be of the order of the Mach number square and  
507 the Mach number, respectively. It is known that some stabilization methods,  
508 alike upwind scheme [27], can produce pressure fluctuations with the wrong  
509 order. The objective of Fig. 6 is to show that the new definition of the viscosity  
510 coefficients yields the correct order in the low Mach limit for both the pressure  
511 and velocity variables. For reference purpose, the function  $f(M) = M^2$  and  
512  $f(M) = M$  are plotted.

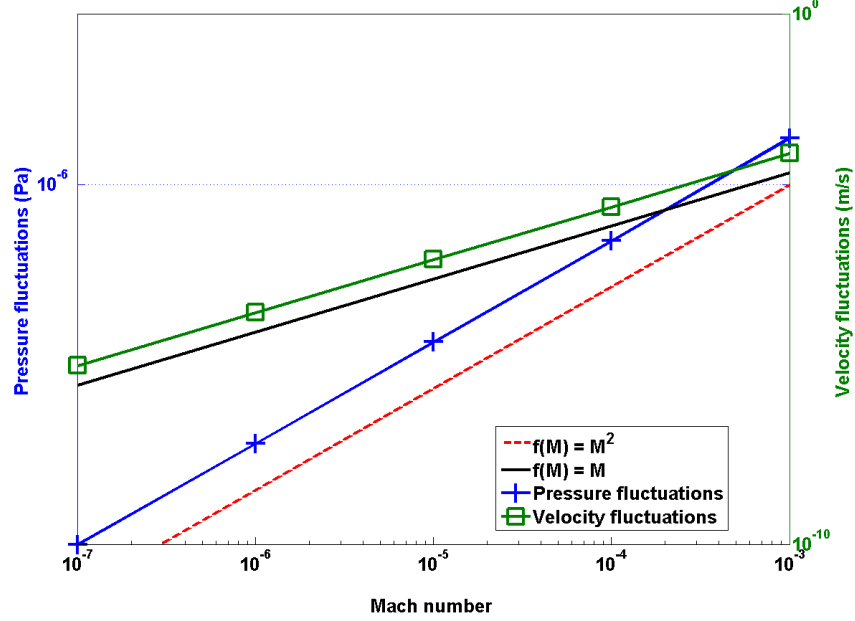


Figure 6: Log-log plot of the pressure and velocity fluctuations as a function of the far field Mach number.

### 5.5. Subsonic flow over a 2-D hump

This is another example of an internal flow configuration. It consists of a channel of height  $L = 1 \text{ m}$  and length  $3L$ , with a circular bump of length  $L$  and thickness  $0.1L$ . The bump is located on the bottom wall at a distance  $L$  from the inlet. The system is initialized with a uniform pressure  $P = 101325 \text{ Pa}$  and temperature  $T = 300 \text{ K}$ . The initial velocity is computed from the Mach number,  $M_\infty$ , the pressure, the temperature and the Ideal Gas equation of state with the heat capacity  $C_v = 717 \text{ J/kg} \cdot \text{K}$  and the heat capacity ratio  $\gamma = 1.4$ . At the inlet, a subsonic stagnation boundary condition is used and the stagnation pressure and temperature are computed using Eq. (26). The static pressure  $P_s = 101325 \text{ Pa}$  is set at the subsonic outlet. A uniform grid is used to get the numerical solution until steady-state is reached. The results are shown in Fig. 7a, Fig. 7b, Fig. 7c and Fig. 7d for the inlet Mach numbers  $M_\infty = 0.7$ ,  $M_\infty = 0.01$ ,  $M_\infty = 10^{-4}$  and  $M_\infty = 10^{-7}$ , respectively. It is expected that, within the low Mach number range, the solution does not depend on the Mach number and is identical to the solution obtained with an incompressible flow code. On the other hand, for a flow at  $M = 0.7$ , the compressible effects become more important and shock can form.



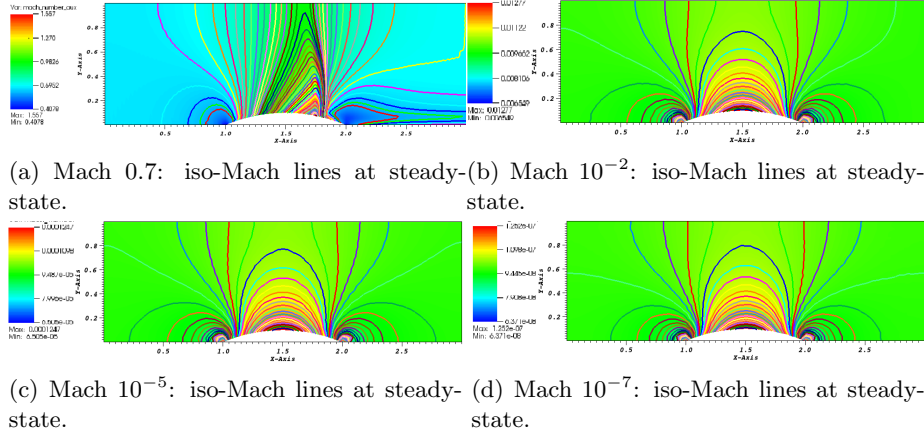


Figure 7: Steady-state solution for a 2-D flow over a circular bump.

531 The results showed in Fig. 7b, Fig. 7c and Fig. 7d correspond to the low  
532 Mach regime. The iso-Mach lines are drawn ranging from the minimum and the  
533 maximum of each legend with 50 intervals. The steady-state solution is sym-  
534 metric and does not depend on the value of the inlet Mach number as expected.  
535 In Fig. 7a, the steady-state numerical solution develops a shock: the compress-  
536 ibility effect are no longer negligible. The iso-Mach lines are also plotted with  
537 50 intervals and ranging from 0.4 to 1.6. The shock is well resolved and does  
538 not display any instability or spurious oscillation.  
539 The results presented in Fig. 7 were obtained with the new definition of the vis-  
540 cosity coefficient (see Eq. (20)), and, illustrate the capabilities of the entropy-  
541 viscosity method to adapt to the type of flow (subsonic and transonic flows)  
542 without using any tuning parameters, but by just evaluating the entropy resid-  
543 ual that is an indicator of the entropy production.

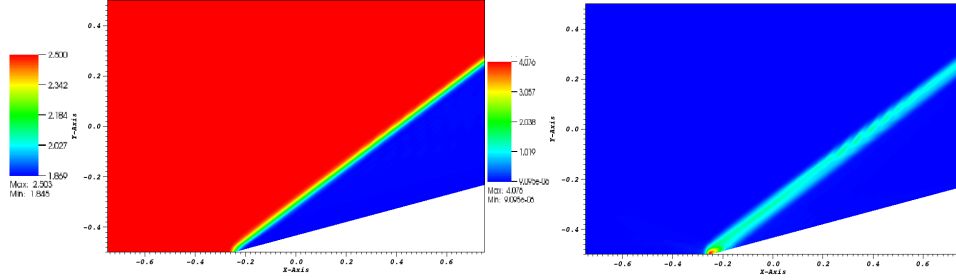
#### 544 5.6. Supersonic flow in a compression corner

545 This is an example of a supersonic flow over a wedge of angle  $15^\circ$  where an  
546 oblique shock is generated at steady-state. The Mach number upstream of the  
547 shock is fixed to  $M = 2.5$ . The initial conditions are uniform: the pressure and  
548 temperature are set to  $P = 101325 \text{ Pa}$  and  $T = 300 \text{ K}$ , respectively. The initial  
549 velocity is computed from the upstream Mach number and using the Ideal Gas  
550 equation of state with the same parameters as in Section 5.5. The code is run  
551 until steady-state. An analytical solution for this supersonic flow is available  
552 and give the downstream to upstream pressure, entropy and Mach number ratios  
553 [14]. The analytical and numerical ratios are given in see in Table 11, and are  
554 very close.

Table 11: Analytical solution for the supersonic flow on an edge eat  $15^\circ$  at  $M = 2.5$ .

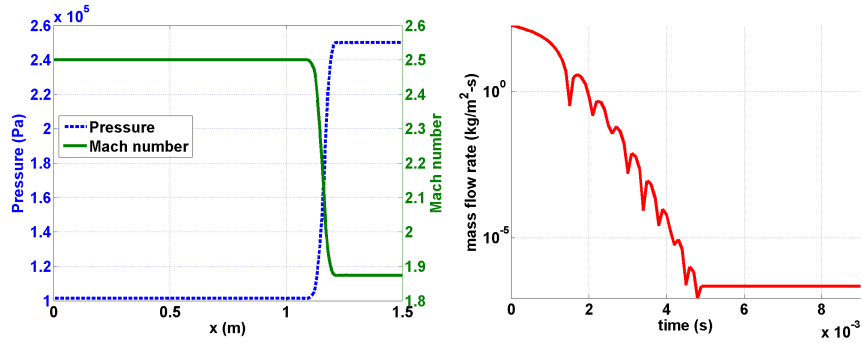
	analytical downstream to upstream ratio	numerical downstream to upstream ratio
Pressure	2.47	2.467
Mach number	0.74	0.741
Entropy	1.03	1.026

555 The inlet is supersonic and therefore, the pressure, temperature and velocity  
556 are specified using Dirichlet boundary conditions. The outlet is also supersonic  
557 and none of the characteristics enter the domain through this boundary: the  
558 values will be computed by the implicit solver.



(a) Mach solution at steady-state.

(b) Viscosity coefficient at steady-state.



(c) Pressure and Mach number profiles at steady-state

(d) Difference between inlet and outlet mass flow rates as a function of time.

Figure 8: Steady-state solution for a flow in a 2-D compression corner.

559 The steady-state numerical solution is given in Fig. 8: the Mach number,  
560 the viscosity coefficients are plotted in Fig. 8a and Fig. 8b, respectively. The  
561 steady-state solution is formed of two regions of constant states, separated by  
562 the oblique shock. In Fig. 8b, the viscosity coefficient is large in the shock,  
563 small anywhere else, and thus, behaves as expected. At the corner of the edge

at  $x = -0.25$  m, the viscosity coefficient is peaked because of the treatment of the wall boundary condition: at this particular node, the normal is not well defined and can cause numerical errors. The 1-D plots of the pressure and the mach number at  $y = 0$ , are also given in Fig. 8c: the shock does not show any spurious oscillations and is well resolved. Finally, the difference between the inlet and outlet mass flow rates is plotted in Fig. 8d and show that the steady-state is reached.

Overall, the numerical solution does not show any oscillations, match the analytical solution, and the shock is well resolved.

## 6. Conclusions

A new version of the entropy viscosity method valid for a wide range of Mach number and applied to the multi-D Euler equations with variable area was derived and presented. The definition of the viscosity coefficient is now consistent with the low Mach asymptotic limit, does not require an analytical expression of the entropy function, and thus, could be used with any equation of state having a convex entropy. Tests were performed with the Ideal and Stiffened Gas equation of states. In 1-D, convergence of the numerical solution (either smooth or with shocks) to the exact solution was demonstrated by computing the convergence rates of the L1 and L2 norms of the error for flows in convergence-divergent nozzle and a straight pipe. 2-D simulations were also performed for both subsonic and supersonic flows, and various geometries: the entropy viscosity method behaves well for a wide range of Mach number. The numerical results obtained for a flow over a circular bump (subsonic and transonic flows) illustrates the capabilities of the method to adapt to the flow type. As future work, the entropy viscosity method will be extended to the 1-D seven equations model [19]. This two-phase flow system of equations is a good candidate for two reasons: it is unconditionally hyperbolic and degenerates to the multi-D Euler equations when one phase disappears.

## Acknowledgments

The authors would like to thank Bojan Popov and Jean Luc Guermond for the many fruitful discussions.

## References

- [1] J. L. Guermond, R. Pasquetti, Entropy viscosity method for nonlinear conservation laws, *Journal of Comput. Phys* 230 (2011) 4248–4267.
- [2] J. L. Guermond, R. Pasquetti, Entropy viscosity method for high-order approximations of conservation laws, *Lecture Notes in Computational Science and Engineering* 76 (2011) 411–418.

- 601 [3] B. Cockburn, C. Johnson, C. Shu, E. Tadmor, Advanced numerical approx-  
 602 imation of nonlinear hyperbolic equations, Lecture Notes in Mathematics  
 603 1697.
- 604 [4] B. Cockburn, G. Karniadakis, C. Shu, Discontinuous galerkin methods:  
 605 theory, computation and applications, Lecture Notes in Computer Science  
 606 and Engineering 11.
- 607 [5] R. Lohner, Applied CFD Techniques: an Introduction based on Finite  
 608 Element Methods, 2<sup>nd</sup> Edition Wiley, 2003.
- 609 [6] A. Lapidus, A detached shock calculation by second order finite differences,  
 610 J. Comput. Phys. 2 (1967) 154–177.
- 611 [7] R. Lohner, K. Morgan, J. Peraire, A simple extension to multidimensional  
 612 problems of the artificial viscosity due to lapidus, Commun. Numer. Meth-  
 613 ods Eng. 1(14) (1985) 141–147.
- 614 [8] J. Donea, A. Huerta, Finite Element Methods for Flow Problems, Oxford  
 615 University Press, 2003.
- 616 [9] H. Guillard, C. Viozat, On the behavior of upwind schemes in the low mach  
 617 number limit, Computers & Fluids 28 (1999) 63–86.
- 618 [10] E. Turkel, Preconditioned techniques in computational fluid dynamics,  
 619 Annu. Rev. Fluid Mech. 31 (1999) 385–416.
- 620 [11] J. S. W. D. L. Darmofal, J. Peraire, The solution of the compressible euler  
 621 equations at low mach numbers using a stabilized finite element algorithm,  
 622 Comput. Methods Appl. Mech. Engrg. 190 (2001) 5719–5737.
- 623 [12] X.-S. Li, C.-W. Gu, An all-speed roe-type scheme and its asymptotic anal-  
 624 ysis of low mach number behavior, Journal of Computational Physics 227  
 625 (2008) 5144–5159.
- 626 [13] J. L. Guermond, B. Popov, Viscous regularization of the euler equations  
 627 and entropy principles, under review.
- 628 [14] J. D. Anderson, Modern compressible flow, in: Guide for Verification and  
 629 Validation in Computational Solid Mechanic., New York, 1982, pp. 10–  
 630 2006.
- 631 [15] J. L. Guermond, R. Pasquetti, Entropy-based nonlinear viscosity for four-  
 632 rier approximations of conservation laws, in: C.R. Math. Acad. Sci., Vol.  
 633 326, Paris, 2008, pp. 801–806.
- 634 [16] V. Zingan, J. L. Guermond, J. Morel, B. Popov, Implementation of the  
 635 entropy viscosity method with the discontinuous galerkin method, Journal  
 636 of Comput. Phys 253 (2013) 479–490.

- 637 [17] E. F. Toro, Riemann Solvers and numerical methods for fluid dynamics,  
638 2<sup>nd</sup> Edition, Springer, 1999.
- 639 [18] B. Perthame, C. W. Shu, On positivity preserving finite volume schemes for  
640 euler equations, Numer. Math. 73 (1996) 119–130.
- 641 [19] R. Berry, R. Saurel, O. LeMetayer, The discrete equation method (dem)  
642 for fully compressible, two-phase flows in ducts of spatially varying cross-  
643 section, Nuclear Engineering and Design 240 (2010) 3797–3818.
- 644 [20] B. Muller, Low-mach number asymptotes of the navier-stokes equations,  
645 Journal of Engineering Mathematics 34 (1998) 97109.
- 646 [21] R. Loubere, Validation test case suite for compressible hydrodynamics com-  
647 putation, Theoretical Division T-7 Los Alamos National Laboratory.
- 648 [22] D. L. Darmofal, K. Siu, A robust multigrid algorithm for the euler equations  
649 with local preconditioning and semi-coarsening, Journal of Computational  
650 Physics 151 (1999) 728756.
- 651 [23] P. Perrot, A to Z of Thermodynamics, Oxford University Press, 1998.
- 652 [24] O. LeMetayer, J. Massoni, R. Saurel, Elaborating equation of state for a  
653 liquid and its vapor for two-phase flow models, International Journal of  
654 Thermal Science 43 (2004) 265–276.
- 655 [25] S. LeMartelot, B. Nkonga, R. Saurel, Liquid and liquid-gas flows at all  
656 speeds: Reference solutions and numerical schemes., Research report 7935.
- 657 [26] R. A. DeVore, G. G. Lorentz, Constructive Approximation, Springer-  
658 Verlag, 1991.
- 659 [27] H. Guillard, C. Viozat, On the behaviour of upwind schemes in the low  
660 mach number limit, Comput. Fluids 105 (1993) 207–233.

661 **A. Derivation of the entropy residual as a function of the density, the**  
 662 **pressure and the speed of sound:**

663 The entropy residual is often expressed as a function of the entropy  $s(\vec{r}, t)$   
 664 as follows:

$$D_e(\vec{r}, t) = \partial_t s(\vec{r}, t) + \vec{u} \cdot \vec{\nabla} \cdot s(\vec{r}, t)$$

665 where all variables were defined previously. This form of the entropy residual is  
 666 not suitable for the low-Mach limit as explained in Section 2.1. It can be shown  
 667 that the entropy residual  $D_e(\vec{r}, t)$  can be recast as a function of the primitive  
 668 variables (pressure, velocity and density) and the speed of sound. This is the  
 669 objective of this appendix.

670 The first step is to use the chain rule, remembering that the entropy is assumed  
 671 function of the internal energy  $e$  and the density  $\rho$ :

$$D_e(\vec{r}, t) = s_e \frac{de}{dt} + s_\rho \frac{d\rho}{dt}$$

672 where  $s_x$  denotes the partial derivative of  $s$  with respect to the variable  $x$ . The  
 673 short-notation  $\frac{d}{dt}$  is used for the total or material derivative. We no need to  
 674 make the pressure appear: this can be achieved by noticing that the internal  
 675 energy is a function of the pressure and the density based on the definition of  
 676 the equation of state. Once again, by using the chain rule, it yields:

$$\begin{aligned} D_e(\vec{r}, t) &= s_e e_P \frac{dP}{dt} + (s_e e_\rho + s_\rho) \frac{d\rho}{dt} \\ &= s_e e_P \left( \frac{dP}{dt} + \frac{1}{s_e e_P} (s_e e_\rho + s_\rho) \frac{d\rho}{dt} \right) \\ &= s_e e_P \left( \frac{dP}{dt} + \left( \frac{e_\rho}{e_P} + \frac{s_\rho}{s_e e_P} \right) \frac{d\rho}{dt} \right) \end{aligned}$$

677 We are now close to the final result (see Eq. (8)). It remains to prove that the  
 678 term multiplying the material derivative of the density is equal to the speed  
 679 of sound square. The speed of sound is often defined as the partial derivative  
 680 of the pressure with respect to the density at constant entropy, which can be  
 681 recast as a function of the entropy as follows (see Appendix A.2 of [13]):

$$c^2 = \left( \frac{\partial P}{\partial \rho} \right)_s = P_\rho - \frac{s_\rho}{s_e} P_e = -\frac{e_\rho}{e_P} - \frac{s_\rho}{s_e e_P}$$

682 using the following relations (see Appendix A.1 of [13]):

$$P_e = \frac{1}{e_P} \text{ and } P_\rho = \frac{e_\rho}{e_P}$$

683 Then, the result follows.

684 **B. Derivation of the dissipative terms for the multi-D Euler equations**  
 685 **with variable area using the entropy minimum principle:**

686 The multi-D Euler equations with variable area are recalled here:

$$\begin{cases} \partial_t (\rho A) + \vec{\nabla} \cdot (\rho \vec{u} A) = 0 \\ \partial_t (\rho \vec{u} A) + \vec{\nabla} \cdot [A (\rho \vec{u} \otimes \vec{u} + P \mathbf{I})] = P \vec{\nabla} A \\ \partial_t (\rho E) + \vec{\nabla} \cdot [\vec{u} (\rho E + P)] = 0 \end{cases}$$

687 Assuming the existence of an entropy  $s$  function of the density  $\rho$  and the internal  
 688 energy  $e$ , the above system of equations admits the following entropy residual  
 689 [17]:

$$A \rho \left( \partial_t s + \vec{u} \cdot \vec{\nabla} \cdot s \right) \geq 0$$

690 when assuming  $P s_e + \rho^2 s_\rho = 0$ . An entropy function  $s$  verifying this equation  
 691 is also a solution of the second thermodynamic law for a reversible system,  
 692  $T ds = de - \frac{P}{\rho^2} d\rho$ , which implies  $s_e = T^{-1} \geq 0$ .

693 In order to apply the entropy viscosity method, dissipative terms are added to  
 694 each equation. Then, the entropy residual is derived again: extra terms due to  
 695 the dissipative terms will appear in the left-hand side. In order to prove the  
 696 minimum entropy principle, these extra terms are either recast as conservative  
 697 term, or shown to be positive.

698 The multi-D Euler equations with variable area with dissipative terms, yield:

$$\begin{cases} \partial_t (\rho A) + \vec{\nabla} \cdot (\rho \vec{u} A) = \vec{\nabla} \cdot f \\ \partial_t (\rho \vec{u} A) + \vec{\nabla} \cdot [A (\rho \vec{u} \otimes \vec{u} + P \mathbf{I})] = P \vec{\nabla} A + \vec{\nabla} \cdot g \\ \partial_t (\rho E) + \vec{\nabla} \cdot [\vec{u} (\rho E + P)] = \vec{\nabla} \cdot h \end{cases} \quad (27)$$

699 where  $f$ ,  $g$  and  $h$  are the dissipative terms to derive. Starting from the modified  
 700 system of equations given in Eq. (27), the entropy residual is derived again:

$$\begin{aligned} A \rho \left( \partial_t s + \vec{u} \cdot \vec{\nabla} \cdot s \right) &= s_e \left[ \vec{\nabla} \cdot h + g \vec{\nabla} u + \left( \frac{u^2}{2} - e \right) \vec{\nabla} \cdot f \right] \\ &+ \rho s_\rho \vec{\nabla} \cdot f \end{aligned} \quad (28)$$

701 The next step consists of choosing a definition for each of the dissipative terms  
 702 so that the left hand-side is proven positive. The right hand-side of Eq. (28)  
 703 can be simplified using the following relations,  $g = A \mu \vec{\nabla}^s \vec{u} + \vec{u} \otimes f$  and  $h =$   
 704  $\tilde{h} + \vec{u} \cdot g - 0.5 ||\vec{u}||^2 f$ , which yields:

$$A \rho \left( \partial_t s + \vec{u} \cdot \vec{\nabla} \cdot s \right) = s_e \left[ \vec{\nabla} \cdot \tilde{h} - e \vec{\nabla} \cdot f \right] + \rho s_\rho \vec{\nabla} \cdot f + A s_e \mu \vec{\nabla}^s \vec{u} \cdot \vec{\nabla} \vec{u}$$

705 The right hand-side is now integrated by part:

$$\begin{aligned} A \rho \left( \partial_t s + \vec{u} \cdot \vec{\nabla} \cdot s \right) &= \vec{\nabla} \cdot \left[ s_e \tilde{h} - s_e e f + \rho s_\rho f \right] - \\ &\vec{\nabla} \cdot \tilde{h} \vec{\nabla} s_e - f \vec{\nabla} (e s_e) - f \vec{\nabla} (\rho s_\rho) + A s_e \mu \vec{\nabla}^s \vec{u} \cdot \vec{\nabla} \vec{u} \end{aligned}$$

706 where  $\vec{\nabla}^s$  is the symmetric gradient. The term  $As_e\mu\vec{\nabla}\vec{u}^s\vec{\nabla}\vec{u}$  is positive and thus,  
 707 does not need any further modification. It remains to treat the other terms of  
 708 the right hand-side that we now call  $rhs$ :

$$rhs = \vec{\nabla} \cdot [s_e \tilde{h} - s_e e f + \rho s_\rho f] - \vec{\nabla} \cdot \tilde{h} \vec{\nabla} s_e - f \vec{\nabla} (e s_e) - f \vec{\nabla} (\rho s_\rho)$$

709 The first term of  $rhs$  is a conservative terms. By choosing carefully a definition  
 710 for  $\tilde{h}$  and  $f$ , the conservative term can be expressed as a function of the entropy  
 711  $s$ . It is also required to include the variable area in the choice of the dissipative  
 712 terms so that when assuming constant area, the regular multi-D Euler equations  
 713 are recovered. The following definitions for  $\tilde{h}$  and  $f$  are chosen:

$$\tilde{h} = A\kappa\vec{\nabla}(\rho e) \text{ and } f = A\kappa\vec{\nabla}\rho,$$

714 which yields, using the chain rule:

$$rhs = \vec{\nabla} \cdot (A\kappa\vec{\nabla}s) - A\kappa \underbrace{\left[ \vec{\nabla}(\rho e)\vec{\nabla}s_e + \vec{\nabla}\rho\vec{\nabla}(e s_e) + \vec{\nabla}(\rho s_\rho) \right]}_{\mathbf{Q}}$$

715 It remains to treat the term  $\mathbf{Q}$  that can be recast under a quadratic form,  
 716 following the work done in [13]:

$$\begin{aligned} \mathbf{Q} &= X^t \Sigma X \\ \text{with } X &= \begin{bmatrix} \vec{\nabla}\rho \\ \vec{\nabla}e \end{bmatrix} \text{ and } \Sigma = \begin{bmatrix} \partial_\rho(\rho^2\partial_\rho s) & \partial_{\rho,e}s \\ \partial_{\rho,e}s & \partial_{e,e}s \end{bmatrix} \end{aligned}$$

717 The matrix  $\Sigma$  is symmetric and identical to the matrix obtained in [13]. The sign  
 718 of the quadratic form can be simply determined by studying the positiveness of  
 719 the matrix  $\Sigma$ . In this particular case, it is required to prove that the matrix is  
 720 negative definite: the quadratic form is in the right hand-side and is preceded of  
 721 a negative sign. According to [13], the convexity of the opposite of the entropy  
 722 function  $s$  with respect to the internal energy  $e$  and the specific volume  $1/\rho$  is  
 723 sufficient to ensure that the matrix  $\Sigma$  is negative definite.

724 Thus, the right hand-side of the entropy residual Eq. (28), are now either recast  
 725 as conservative terms, or known to be positive. Following the work done by [13],  
 726 the entropy minimum principle holds.